Fluorescent Mechanism of a Highly Selective Probe for Copper(II) Detection: A Theoretical Study

Huixue Li,* Xiaofeng Wang, Kun Yuan, Lingling Lv, Kui Liu, and Zhifeng Li*

Read Online

ACCESS | Metrics & More | Article Recommendations | Supporting Information

ABSTRACT: A highly selective probe for copper(II) detection based on the dansyl group was theoretically studied by means of (time-dependent) density functional theory. The calculated results indicated that the oscillator strength of the fluorescent process for the probe molecule is considerably large, but the counterpart of its copper(II) complex is nearly zero; therefore, the predicted radiative rate k_r of the probe is several orders of magnitude larger than that of its complex; however, the predicted internal conversion rate k_{ic} of both the probe and its complex is of the same order of magnitude. In addition, the simulated intersystem crossing rate k_{isc} of the complex is much greater than that of the probe due to the effect of heavy atom from the copper atom in the complex. Based on the above information, the calculated fluorescence quantum yield of the probe is 0.16% and that of the complex becomes 10^{-6}%, which implies that the first excited state of the probe is bright state and that of the complex is dark state. For the complex, the hole−electron pair analysis indicates that the process of $S_0 \rightarrow S_1$ belongs to metal-to-ligand charge transfer; its density-of-state diagram visually illustrates that the highest occupied molecular orbital (HOMO) contains the ingredient of the s orbital from the copper atom, which decreases the frontier orbital energy level and the overlap integral of HOMO and LUMO.
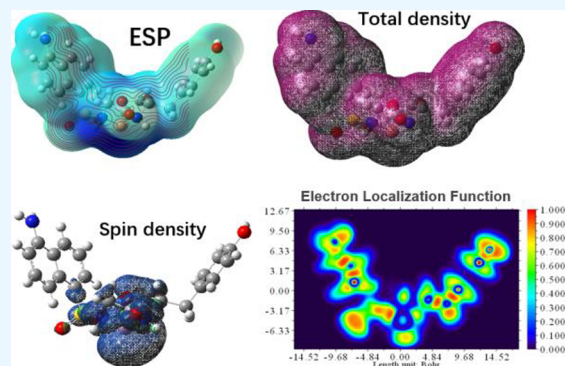
1. INTRODUCTION

Copper is an essential transition metal element in organisms, and it is the third most abundant element in the human body after iron and zinc.[1] Usually, it is in the form of divalent copper (Cu^{2+}) and mainly exists in ceruloplasmin (CP), which plays a vital role in erythropoiesis, central nervous system, and enzymatic activity.[2,3] Brain development in children will be affected seriously when Cu^{2+} is insufficient, and conversely, when Cu^{2+} concentration in the body exceeds the normal range, highly reactive hydroxyl radicals can come into being and hinder cell metabolism. In addition, certain neuro-degenerative diseases are proven to be closely related to the destruction of copper homeostasis. Moreover, abnormal copper metabolism may interfere with the synthesis of CP and cause liver cirrhosis and Wilson disease.[1,4] Copper can also influence iron metabolism and hematopoietic function, further affecting the central nervous system, bone tissue metabolism, endocrine and cardiovascular systems, and energy metabolism.[5] Hence, there is an immediate need to develop an accurate and convenient method to detect Cu^{2+} in environmental and biological samples.[6,7] Fluorescent probes are widely used for detecting certain compounds or ions,[2,8] where the color or fluorescence intensity changes obviously upon encountering and interacting with analytes.[3,9] Over the past decade, fluorescent probes are considered as ideal tools to monitor diverse chemical and biological species, and they have

been greatly developed in the field of theory and application.[10] There are many benefits to detect compounds or ions using fluorescent probes, such as high sensitivity, fast response, simple process, and low cost.[1,11] Until now, rhodamine, coumarin, and fluorescein derivatives as fluorescent probes for detecting Cu^{2+} have been successfully synthesized based on effective fluorophores,[12] and these derivatives will react chemically with Cu^{2+} by bond cleavage reaction, ring-opening reaction, or hydrolysis reaction. The coordination between recognition sites of probes and Cu^{2+} changes the electronic distribution of the fluorophores, leading to distinct fluorescence emission shifts or intensity changes.[13]

In addition, researchers investigated the interactions between probe molecules and their target species. Simultaneously, the electronic excited states of fluorescent probes were calculated to elucidate their fluorescence properties, and a series of fluorescence-based sensing mechanisms were proposed consequently.[14,15] Up to now, advances in

a: optimized S_0 state for the ligand

b: Schematic diagram of the ligand

c: optimized S_0 state for the complex

d: Schematic diagram of the complex

e: the atomic symbols and labels in the ligand

f: the atomic symbols and labels in the complex

g: the schematic diagram of ligand molecule

h: the schematic diagram of complex molecule

Figure 1. Bond parameters of the studied molecules in their minima, the ligand by B3LYP/6-31G(d,p), and the complex by B3LYP/Gen.

calculation methods, computational power, and modeling software have provided useful help to explain easily experimental fluorescence phenomena by excited-state theoretical simulations.[15,16]

Li and Wang synthesized a fluorescent probe to monitor Cu^{2+} based on the dansyl group[7] in order to improve solubility in complete aqueous solution. They introduced an oligopeptide to the dansyl group, which can offer multiple N and O atoms to chelate metal ions and promote its dissolution. This probe (Figure 1) can supply chelating sites for Cu^{2+} and display a high selectivity toward Cu^{2+} in the aqueous solution, it can work effectively in a wide pH span from 6 to 12 via a fluorescence "turn-off" manner, and an association constant of 6.47×10^4 M^{-1} between the probe and Cu^{2+} was determined experimentally. However, the vertical excitation energy, the excited-state geometrical optimization, the photophysical properties, and the excited-state dynamics of this probe were not done theoretically. In this paper, we attempt to provide molecular-level explanations based on time-dependent density functional theory (TDDFT). By conducting theoretical studies of fluorescence probes, one can gain a deeper understanding of the fundamental principles and mechanisms involved in ion recognition. The results can then be used to guide the selection of ideal receptor molecules, improve the device performance, and provide a framework for the rational design of new fluorescent sensors. As such, theoretical studies are essential for advancing the field of ion recognition and accelerating the development of practical applications for fluorescent sensors.

2. THEORETICAL METHOD AND COMPUTATIONAL DETAILS

In view of the fact that the dansyl probe molecule does not have available single-crystal structure data to utilize, we employed the Molclus program to screen the most likely geometry with the lowest energy.[17] Taking into account the probe being a soluble sodium salt, it will ionize in water solution to release the sodium ion and the probe anion. Therefore, the isomers of the probe anion were only generated randomly by Gentor, and more than 1700 were obtained. Then each initial structure was optimized to a local minimum with the semiempirical method PM7 using MOPAC program.[18] The optimized isomers were compiled and listed according to energy. The 50 lowest-lying were selected as candidate structures and further optimized with density functional theory using the Gaussian 16 software package.[19] All atoms were dealt by the B3LYP hybrid functional with the 6-31G(d,p) basis set. It was found that there was no change in the rankings for these low-lying isomers based on the recalculated energy. Then, the global minimum was finally identified for this fluorescent probe. Moreover, to further verify that the optimized structures at the functional B3LYP level are indeed global minima, another functional ωB97XD with the same basis set was applied to optimize the geometries and calculate the relative energies. The lowest-lying structures at the ωB97XD level were approximately identical to these B3LYP results, and only a few ignorable deviations of bond lengths and angles were found (see Figure S2). The frequency of global minimum geometry was computed at the same level, and no imaginary frequencies were found.

Table 1. Absorption and Emission Data of the Title Compound According to TDDFT Calculations, Together with the Experimental Data

method	oscillator strength	main configuration	assignment	λ_{cal} (nm)	λ_{exp} (nm)
predicted maximum emission wavelength of L					
B3LYP/def2SVP	0.1010	HOMO → LUMO	0.7044	542.3	558
B3LYP/6-31G(d,p)	0.1029	HOMO → LUMO	0.7006	541.2	
ωB97XD/6-31G(d,p)	0.1039	HOMO → LUMO	0.7022	442.8	
predicted maximum emission wavelength of LCu					
TPSS/Gen	0.0111	129B → 130B	1.4223	6405.1	
ωB97XD/Gen	0.0003	129B → 130B	0.9852	784.1	
B3LYP/Gen	0.0028	129B → 130B	0.9992	9945.7	
PBE/Gen	0.0608	125B → 129B	0.8746	4727.1	
Cam-B3LYP/Gen	0.0002	129B → 130B	0.9928	937.1	
predicted maximum absorption wavelength of L					
B3LYP/6-31G(d,p)	0.0834	HOMO → LUMO	0.6975	374.6	337
B3LYP/def2SVP	0.0839	HOMO → LUMO	0.6973	377.0	
B3LYP/cc-pvdz	0.0810	HOMO → LUMO	0.6975	373.2	
ωB97XD/6-31G(d,p)	0.1452	HOMO → LUMO	0.6966	323.6	
predicted maximum absorption wavelength of LCu					
TPSS/Gen	0.0166	130A → 131A	0.8536	609.4	
B3LYP/Gen	0.0870	130A → 131A	0.5658	449.3	
		129B → 131B	0.6977		
ωB97XD/Gen	0.1833	130A → 131A	0.6451	378.2	
		129B → 131B	−0.5512		

For the system formed by the transition metal Cu(II) and the probe anion, it was calculated using the unrestricted open-shell method (UB3LYP), and in which the copper atom was treated with the B3LYP/SDD technique,[20] the other non-metal atoms were dealt with B3LYP/6-31G(d,p). The complex conformation searching was similar to that of the probe molecule by Molclus program. Their geometric structures were further optimized in quantum mechanics. The stable complex with the lowest energy was screened out, in which the frequency analysis was carried out at the same level based on the optimized structure to ensure no imaginary frequencies. In addition, the polarizable continuum model (PCM) was employed to simulate the solvent effect in solution.[21]

Finally, the absorption and emission spectra and excited-state calculations were performed by TDDFT at the B3LYP/Gen [Gen refers to the Cu atom employing pseudo-potential SDD, the other atom employing 6-31G(d,p)] theoretical level. The correlative postprocessing calculation, with the internal conversion rate k_{ic}, the intersystem crossing (ISC) rate k_{isc}, and the radiative rate k_r of the title compounds in detail, was implemented by utilizing MOMAP software.[22] MOMAP is a suite of codes developed by the Shuai group for the study of spectroscopy and radiative and nonradiative processes in polyatomic molecules. At present, it is widely used in the research of OLED luminescence and transfer mechanism, organic display and lighting materials, organic solar cells, and organic light communication. This program has been proven to be precise and efficient to predict the photoelectric properties of materials in numerous cases.[23,24]

3. RESULTS AND DISCUSSION

3.1. Optimization Structures of the Probe and Its Complex. Considering that the probe molecule is a strong electrolyte, it will dissociate into a cation (Na$^+$) and an anion (ligand, for short L) in aqueous solution. Hence, we only concentrated on the study about the configurations of the ligand. The optimized and screened geometries of L and its

Cu(II) complex are shown in Figure 1. The anionic geometry of L is a cage-type structure, and the phenol moiety, the naphthylamine dansyl moiety, and the dipeptide moiety are the three walls of this cage. One can find O31 in the carboxy, and H19 in the amino obviously forms a H-bond with 1.998 Å length. It is so strong that the original coplanar-naphthyl is twisted into the nonplanar structure, the dihedral angle of one benzene ring belonging to the naphthyl moiety becomes 11.5°, and the other becomes 9.2° (see Supplementary Information); unsurprisingly, the conjugated π bond spreading on the naphthyl ring will be weakened slightly.

In the optimized structures of the complex consisting of L and Cu^{2+}, the five isomers have the lowest energy and were picked out. The ligand provides carboxy, sulfuryl, and amino as endogenous metal-chelating sites. When the temperature is set as 300 K, the percentage of each configuration is calculated statistically according to Boltzmann distribution. The structures and energies of these isomers are shown in the Supporting Information in detail. We found that the most stable configuration accounts for over 99%, in which the transition metal Cu(II) is close to both the N atoms of the dipeptide and both the O atoms from the carboxy and the dansyl, respectively; that is, the ligand is coordinated with the metal atom in a tetradentate manner in the complex. As a result, the empty orbitals of Cu^{2+} can receive enough lone-pair electrons to strengthen the coordinate bonds and feedback bonds in this system. In order to minimize the repulsion effect, the ligand is switched from a cage to a "V"-shape in cooperation. The computational results indicated that the formation of the coordinate bonds was accompanied by the breaking of the intramolecular H-bond O31−H19. At the same time, the twisty naphthyl ring in the ligand becomes completely planar spontaneously, which implied that the increase of inner energy owing to the hydrogen bond breaking is smaller than the decrease of inner energy owing to coordinate bond forming.

Figure 1 shows that the coordinate bonds O31−Cu52 and O21−Cu52 are 1.837 and 2.139 Å in length, respectively. The former is evidently longer than the latter, which is because the strong electrostatic interaction comes from the O31 atom in the carbonyl with a negative charge and the central Cu^{2+} with a positive charge; however, there exists only covalent interaction between the O21 atom in the dansyl group and the central cation Cu^{2+}. The O21 provides a lone pair electron and Cu^{2+} provides an unoccupied atomic orbital to form a feedback π^* bond, which results in charge transfer between the ligand and the central atom. The coordinate bonds N24−Cu52 and N47−Cu52 are 2.044 and 2.104 Å in length, respectively. We found that O25, N24, and C23 are coplanar and form a local conjugated π system. The lone-pair electron of the O25 atom will transfer to the N24 atom with the aid of conjugation effect. Accordingly, the electron density between N24 and Cu52 atom will enlarge and the corresponding bond order will strengthen. In contrast, the N47 atom has no conjugate condition, and the bond length of N24−Cu52 is slightly shorter than that of N47−Cu52.

Compared to the ligand L, the distance (1.309 Å) of O31−C29 in the complex becomes longer (but 1.262 Å in L), nevertheless, the distance of O30−C29 becomes shorter (1.215 Å in the complex, 1.244 Å in L). As expected, this difference between both the O−C bonds is due to the transfer of electron pair in the carboxyl, that is, the electron in the O31 atom moves to the central metal atom, which makes the electron cloud spreading on the O31−C29 bond reduce and the bond order weaken. Simultaneously, the lone pair electron on the O30 atom shifts to the O30−C29 bond and increases its electron density and bond order. Similarly, both O21−S20 and O22−S20 are 1.469 Å in L, but in the complex, O21−S20 is elongated to 1.499 Å and O22−S20 is shortened to 1.456 Å.

3.2. Photophysical Properties and Reorganization Energy. We used the pseudopotential basis set SDD for the copper atom, the 6-31G(d,p) basis set for non-metal atoms, and associated B3LYP hybrid functional to obtain the first excited state of the L and its complex. No imaginary frequencies showed that both the first excited states are stable configurations. The following calculations based on their optimized geometries of the ground and excited states were performed with TPSS,[25] Cam-B3LYP,[26] ωB97XD,[27] and PBE functionals[28] to assess the absorption and emission properties. Further, the luminous mechanism has been explored with the quantum dynamical model. The transition energy, the oscillator strength (f), the main configuration, and the assignment for the studied systems are listed in Table 1.

Prediction of the first maximum absorption wavelength of the ligand was 323.6 nm with ωB97XD/6-31G(d,p), which exactly matched with the observed 337 nm in the solution. The highest occupied molecular orbital (HOMO) → lowest unoccupied molecular orbital (LUMO) is the main transition configuration in the excited process. More visually, the frontier molecular orbital diagrams (Figure 2) illustrate that the electron transition occurs on the naphthylamine moiety when the ground state is excited by incident light. In comparison, the other functionals and basis sets gave greater deviations from the experimental value. Analogously, the calculated maximum absorption wavelengths of the complex with ωB97XD/SDD were 378.2 nm and obviously better than that from the other functionals. The calculated results as well indicated that the main configurations include both 130A → 131A (the assignment coefficient is 0.6451) and 129B → 130B
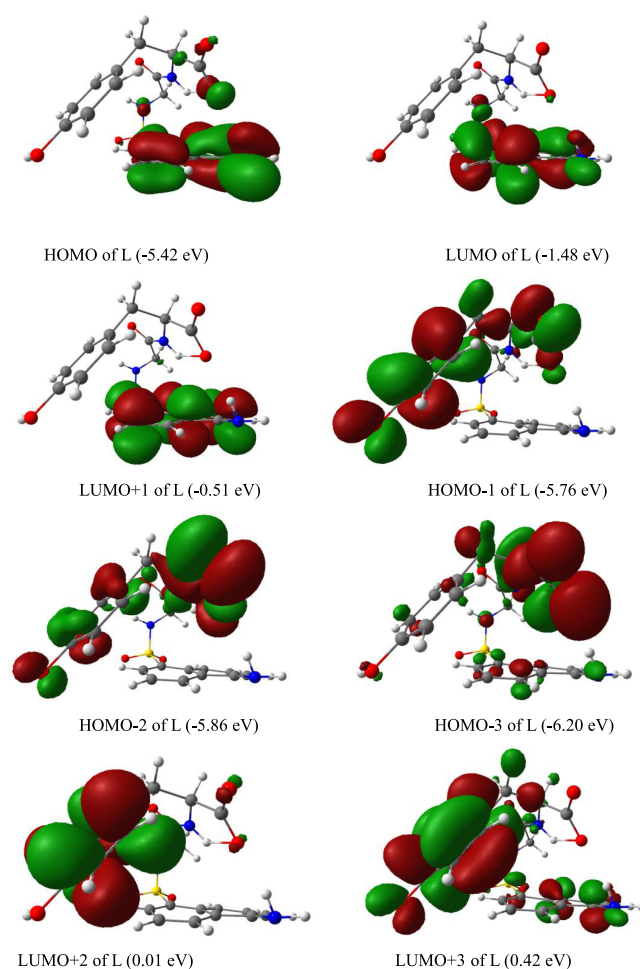

Figure 2. Frontier molecular orbital diagrams of the ligand and the complex (isovalue = 0.02).

(the assignment coefficient is −0.5512). The former exhibits local excitation characteristic, and the latter has charge-transfer characteristic (Figure 3). In addition, both the simulated oscillator strengths were close to each other (0.1452 for the ligand and 0.1833 for the complex).

For the emission process, we observed that the simulative emission peak of L is 542 nm in aqueous solution by B3LYP/6-31G(d,p) and is basically consistent with the experimental result (558 nm). The frontier molecular orbitals (Figure 2) show that this electron transition has a distinct local transition characteristic. The dominant transition configuration in this process is from HOMO to LUMO, and thus the B3LYP functional is more suitable to simulate the emission process. However, the simulative value by ωB97XD/6-31G(d,p) has an even larger variation (442.8 nm) comparatively. As known to all, the ωB97XD functional is a long-range corrected hybrid functional that includes a range-separation parameter to accurately describe both short-range and long-range electron−electron interactions. When ω is set to 0.0522 $Bohr^{-1}$, the calculated maximum emission wavelength is 514 nm, which is greatly improved compared with the former. It must be emphasized that the first excited state of the L molecule is a bright state theoretically with considerable oscillator strength (0.1029), nevertheless, for the emission process of the complex, our computed results demonstrated that ωB97XD associated with the pseudo-potential basis set has the most plausible results compared to other functionals and sets. The

130A of LCu (-5.91 eV) 131A of LCu (-5.84 eV)

129B of LCu (-6.52 eV) 130B of LCu (-5.88 eV)

131B of LCu (-3.81 eV) 132A of LCu(-2.63 eV)

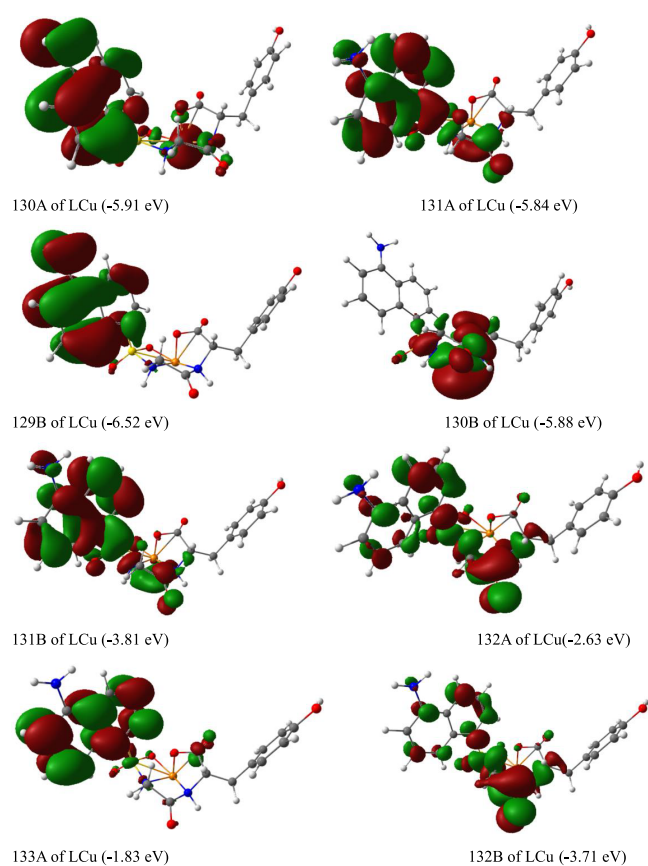133A of LCu (-1.83 eV) 132B of LCu (-3.71 eV)

Figure 3. Frontier molecular orbital diagrams of the complex (isovalue = 0.02).

relevant oscillator strength was only 0.0003 (corresponding emission peak 784.1 nm), which manifested that the first excited state was a dark state (the absorption and emission spectra of both the probe and its complex are shown in Figure 4), as well as the data by Cam-B3LYP, B3LYP, TPSS, and PBE functionals confirmed the above conclusion, that is, all oscillator strengths were very small and nearly zero. Meanwhile, all functionals verified that the main transition configuration in the emission process of the complex is 129B → 130B. We found that the characteristic of charge transfer from the ligand to the Cu^{2+} cation is pretty evident through the molecular orbital (MO) diagrams. Therefore, the long-range

corrected functionals[29] ωB97XD and Cam-B3LYP perform better at emission calculation than the others. This means that the overlap integral of both the MOs 129B and 130B is very small, which determines that the corresponding oscillator strength is tiny too. Moreover, to assess the fluorescence quantum yields of both the compounds, we explored the radiative rate k_r, the internal conversion rate k_{ic}, and the ISC rate k_{isc}. Based on these data, the fluorescence quantum yield can be expressed as $\eta = k_r/(k_r + k_{ic} + k_{isc})$.[23] Visibly, k_{ic} and k_{isc} increase, and the fluorescence efficiency will decrease. In contrast, the larger the k_r, the larger the fluorescence efficiency. These factors are strongly correlated with how the fluorescence probe works.

The frequencies of vibrational modes in the S_1 states, the reorganization energy (λ_{reorg}), and the nonadiabatic coupling term (R) are associated closely with the radiative decay rates and internal conversion rate. These parameters involved in the dynamics of the related ground state and excited state were computed theoretically using MOMAP program. All data are compiled and showed in Table 2.

We noticed that the total reorganization energy (λ_{reorg}) for the ligand is 4740 cm^{-1} (i.e., 0.5877 eV) in the fluorescence process. The four-point approach was employed to calculate again in order to verify its credibility.[30] The result (0.5507 eV) indicated that both λ_{reorg} were close to each other. Thus, the thermal vibration correlation function formalism is very reliable. In a similar way, the total λ_{reorg} of the complex is 0.1247 eV by the four-point approach and 0.1447 eV (i.e., 1167 cm^{-1}) by the MOMAP program. Both the simulated results also coincided with each other. Obviously, the total λ_{reorg} of $S_1 \rightarrow S_0$ for the complex is smaller in comparison with the ligand. It is about a quarter the size of the ligand, which is mainly due to the following two reasons. On the one hand, the carbonyl oxygen, the dansyl oxygen, and both the amino nitrogens bond with the central copper cation(II) by coordinate bonds in the complex. The strong interaction between the ligand and the central atom can increase molecular rigidity. More importantly, the newly formed bonds can constrain these atoms in motion and decrease the molecular deformation in the photophysical process, thereby diminishing the corresponding λ_{reorg}. On the other hand, the intramolecular hydrogen bond in the ligand makes the naphthyl ring distort slightly, which reduces the conjugation extent of the π system. On the contrary, the naphthyl ring in the complex relaxes completely, and all atoms are in the same

a: the absorption spectrum
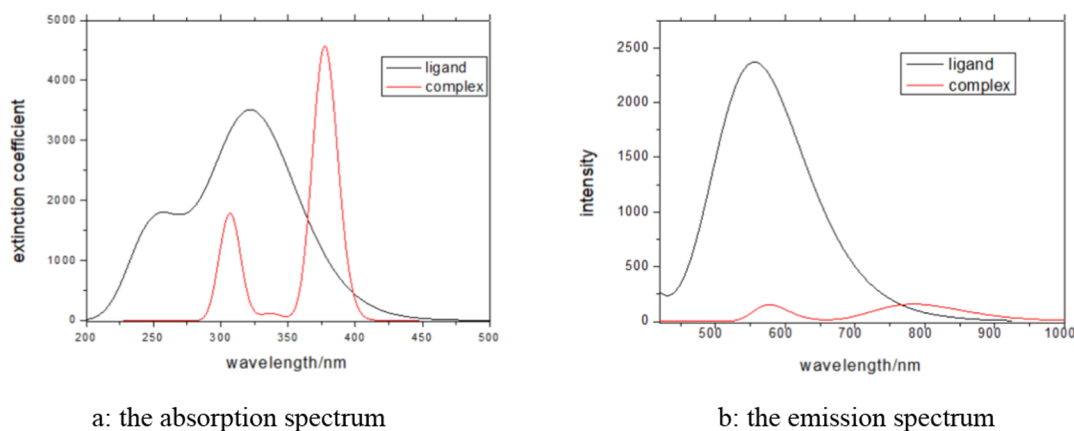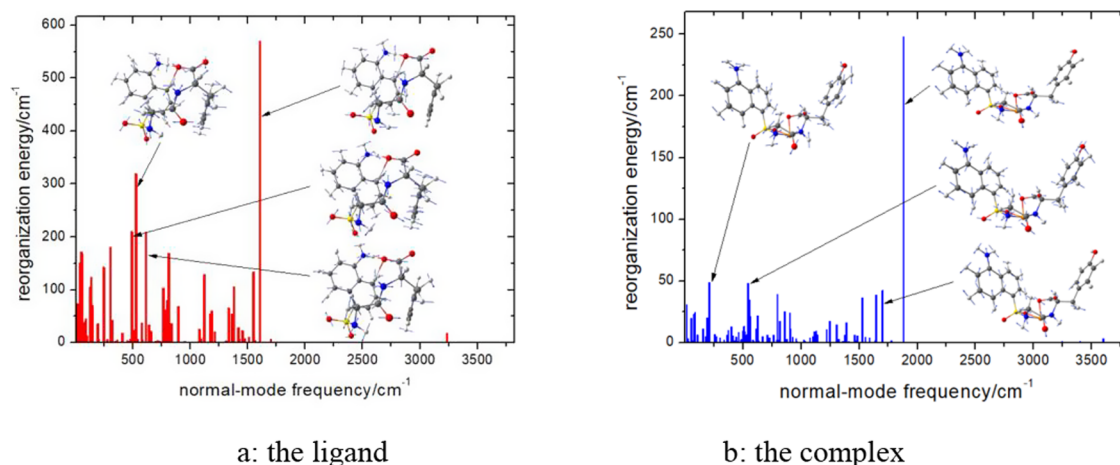

b: the emission spectrum

Figure 4. Absorption and emission spectra of both the probe and its complex.

Table 2. Selected Frequencies of S₁ State, Reorganization Energy (λ_{reorg}/cm⁻¹) by NMA Method in $S_1 \rightarrow S_0$ Process and Nonadiabatic Coupling Term (R)

	ligand				complex		
	freq./cm⁻¹	λ_{reorg}/cm⁻¹	R/cm⁻¹		freq./cm⁻¹	λ_{reorg}/cm⁻¹	R/cm⁻¹
ν_{122}	1607.3	570.6	93.25	ν_{130}	1882.3	248.02	397.01
ν_{41}	525.3	319.2	13.88	ν_{17}	211.6	48.85	93.74
ν_{40}	523.3	223	10.25	ν_{42}	544.7	48.34	146.01
ν_{37}	489.4	209.9	0.49	ν_{128}	1700.9	42.51	73.2
ν_{48}	613	209	24.65	ν_{60}	798.1	39.38	166.92
ν_{24}	303.7	180.4	3.43	ν_{126}	1645.1	38.82	165.9
ν_5	52.5	172	8.48	ν_{120}	1526.3	36.72	101.91
ν_{63}	813.4	169	27.63	ν_{43}	558.5	34.87	21.22
ν_6	58.2	168	0.76	ν_1	16	31.07	27.89
ν_2	36	151.3	1.26	ν_{66}	858.3	25.21	156.08
ν_{20}	246.4	143	17.03	ν_8	88.5	24.48	12.28
ν_{119}	1550.9	134.1	22.12	ν_{70}	905.2	24.04	219.91
ν_{86}	1123.6	128.4	19.26	ν_7	80.1	23.28	71.4
ν_{13}	138	123.2	0.15	ν_{49}	626.5	21.92	20.85
ν_{107}	1379.8	106.1	43.49	ν_{44}	563.1	21.42	10.38
ν_{12}	130.5	105.7	7.37	ν_{15}	193.8	20.38	65.46
ν_{59}	766.6	103.3	25.35	ν_5	54.5	19.92	12.23
ν_{84}	1120	100.6	15.26	ν_{62}	819.6	17.42	71.63

a: the ligand   b: the complex

Figure 5. Calculated reorganization energies of the title compounds versus normal-mode frequency at the S_1 potential energy surface; the inset shows the vibrational displacement vectors corresponding to the first four largest λ_{reorg}.

Table 3. Calculated Radiative Decay Rate (k_r) and Internal Conversion Rates and ISC Rates (k_{ic}) from S_1 to S_0 and the Corresponding Fluorescence Quantum Yield (η) at 300 K for the Probe and its Complex[a]

	radiative decay rate (k_r)	internal conversion rate (k_{ic})	ISC rates (k_{risc})	quantum yield (η)
ligand	7.36×10^8 s⁻¹	4.62×10^{11} s⁻¹	2.21×10^5 s⁻¹	0.16%
complex	2.58×10^3 s⁻¹	2.26×10^{11} s⁻¹	3.17×10^{10} s⁻¹	1.0×10^{-6}%

[a]SOCis 0.277 cm⁻¹ for the ligand and 40.3 cm⁻¹ for the complex using BDF code.

plane, which manifests that the naphthyl in the complex possesses an ideal π-conjugated characteristic and should help to reduce the λ_{reorg}.

To further understand the reorganization energies of $S_1 \rightarrow S_0$, the total λ_{reorg} of the ligand and the complex are projected into each vibration mode of their first excited state. Figures 5a,b graphically show that the low-frequency and middle-frequency vibration modes contribute more to the reorganization energies. We noticed that the largest reorganization energy (248 cm⁻¹) of the complex is from the antisymmetric stretching vibration mode of the carbonyl group with frequency 1882 cm⁻¹, followed closely by the bending

vibration of the C−C−C bond in the alkyl chain with frequency 211.7 cm⁻¹, and it brings about 48.8 cm⁻¹ reorganization energy. Also, both the vibration modes with frequency 1700.9 and 544.7 cm⁻¹ can bring about 42.5 and 48.3 cm⁻¹ reorganization energies, respectively. As far as the ligand is concerned, the first four vibration modes, which produce the largest reorganization energy (570.6, 319.2, 223.1, and 210 cm⁻¹) become 1607.4, 525.3, 523.3, and 489.4 cm⁻¹, respectively, and they are associated with the in-plane stretching vibration of the naphthyl ring, the in-plane deformation vibration of the naphthyl ring, the out-plane distortion vibration of the naphthyl ring, and the in-plane

rocking vibration of the naphthylamine. It should be pointed out that the first four largest λ_{reorg} are in connection with the twisted naphthyl ring in the ligand, which obey the decision making as described above.

3.3. Radiative Decay Rates, Internal Conversion Rates, and ISC Rates.

The radiative and nonradiative decay rates of both the ligand and its complex in Table 3 belong to dynamic parameters, which can provide assistance to investigate the fluorescence quantum yield and fluorescent mechanism. One can observe the following: (i) When taking into account the temperature and vibration modes, the calculated k_r is 7.36×10^8 s^{-1} for the ligand and 2.58×10^3 s^{-1} for the complex at 300 K in aqueous solution. When the temperature and specific molecular vibration are not considered, the radiative decay rates can be computed based on the formula $k_r \approx \frac{f\nu_{fi}^2}{1.5}$; here f is the oscillator strength and ν_{fi} refers to the transition energy; k_r is 2.29×10^7 s^{-1} for the ligand and 3.25×10^4 s^{-1} for the complex. In this way, due to the tiny oscillator strength (0.0003) of the complex, we discovered that k_r for the ligand is always several orders of magnitude larger than that of the complex whether or not considering temperature and molecular vibration; (ii) the predicted k_{ic} is 4.62×10^{11} s^{-1} for the ligand and 2.26×10^{11} s^{-1} for the complex. Both the k_{ic} are of the same order, but the former is about twice that of the latter. Generally, the larger the reorganization energy, the greater the nonadiabatic vibronic coupling between the two states. Accordingly, the internal conversion decay rate becomes faster. As mentioned above, the coordinate bonds in the complex enhance the molecular rigidity and decrease the organization energy of $S_1 \rightarrow S_0$. Therefore, the energy dissipating rate of the complex is less than that of the ligand by nonradiative means. (iii) According to well-known Jablonski diagrams, ISC is another pathway of energy dissipation. The spin−orbital coupling (SOC) between the single state and triple state plays a vital role in this process. Owing to the effect of heavy atom from the copper atom in the complex, its SOC value (40.3 cm^{-1}) is more than dozens of times that of the ligand (0.277 cm^{-1}). Together with the influence from the thermal vibration correlation function, the simulated k_{isc} is 2.21×10^5 s^{-1} for the ligand and 3.17×10^{10} s^{-1} for the complex. The latter is 5 orders of magnitude larger than the former. (iv) Because k_r for the ligand is much greater than that of the complex, whereas both the k_{ic} are close to each other. Meanwhile, the k_{isc} of the ligand and complex are smaller than its k_{ic}. Based on the given information, the calculated fluorescence quantum yield η of the ligand is 0.16%, which is less than its experimental value of 4.7%. Despite being lower, it is still significantly higher than the quantum yield of the complex (1.0×10^{-6}%). The simulated fluorescence quantum yield of the ligand and its complex shows that the ligand exhibits detectable emission band corresponding to the $\pi \rightarrow \pi^*$ transition at 541 nm. Nevertheless, the complex cannot exhibit fluorescence experimentally owing to the tiny radiative rate and considerable nonradiative rates. Due to the defects of the solvation effect model, the displacement harmonic oscillator model used in the thermal vibration correlation function, and certain deviation of the density functional and basis set used in the calculation, there are large errors between the calculated η and the experimental values.

3.4. Hole−Electron and Density-of-State Analysis.

We found that the electronic excitation of the complex cannot be simply depicted as a transition between a specific pair of MOs;

for example, there are two main configurations for the electronic transition of $S_0 \rightarrow S_1$: one is 130A → 131A with coefficient 0.6451, and the other is 129B → 131B with coefficient −0.5512, so it is inconvenient to study their underlying characteristics. This puzzle can be conquered easily by employing the hole−electron analysis method which was suggested by Lu and Chen.[31] The involved electronic structure analyses can also be performed with the Multiwfn 3.8 (dev) code.[32,33] Figure 6b clearly depicts that in the $S_0 \rightarrow S_1$ exciting

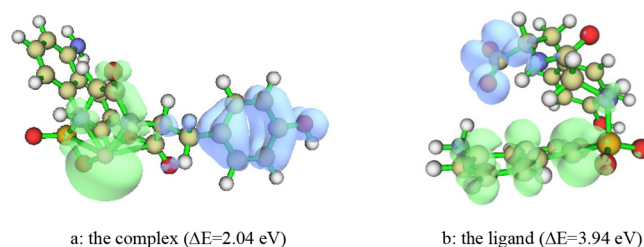a: the complex (ΔE=2.04 eV)   b: the ligand (ΔE=3.94 eV)

Figure 6. Hole and electron distributions of the ligand and its complex: $S_0 \rightarrow S_1$ excitation (isovalue = 0.002). Green and blue regions denote the hole and electron distributions, respectively. ΔE is the energy difference between the HOMO and the LUMO.

process of the ligand, the excited electron leaves the π bonding orbital located on the naphthalene ring and arrives at the π^* antibonding orbital on the carbonyl. Thereby, we can predict that in the S_1 state, the C−C bonds in the naphthalene ring and the C=O bonds in the carbonyl become longer and weaker than those in the S_0 state. Besides, the calculated distance between the centroids of hole and electron is 5.154 Å, and the simulated Coulomb attractive energy is 2.80 eV. Moreover, the calculated intrinsic interfragment charge transfer via the IFCT method is 79.2%.[32,33] Also, Figure 6a shows the $S_0 \rightarrow S_1$ excitation characteristic of the complex by the hole−electron analysis method. Its hole is concentrated on the Cu(II) and the surrounding coordinate atoms of the ligand, and the electron mainly distributes on the benzene ring. In other words, in the exciting process, the Cu atom provides electron to the antibonding orbital of the benzene ring to form a hole−electron pair. The calculated distance between the centroids of hole and electron is 5.967 Å. We also obtained the corresponding Coulomb attractive energy of 2.24 eV by Multwfn code. In addition to this, the intrinsic interfragment charge transfer is 53.6% via the IFCT method. One can see that the absolute amount of charge transfer of the complex is much smaller in contrast with that of the ligand; consequently, the electrostatic interaction between the hole−electron pair in the complex is weaker than that in the ligand. We can anticipate that the released amount of energy for the ligand will be greater than that of the complex when the hole and electron spontaneously recombine, which just happens to be in accordance with the computed emission wavelengths of both the ligand and its complex.

The newly formed coordination bonds in the complex molecule can strengthen the tie between the Cu atom and the ligand atoms. In order to get an intuitive understanding of the coordination bonds and MO characteristic, we plotted the density-of-state (DOS) diagrams of the ligand and its complex.[31,33] DOS can visually manifest energy level distribution of MOs in a chemical system, and the value of the DOS curve demonstrates the number of MOs in the unit energy interval. In Figure 7, we noticed that the total DOS
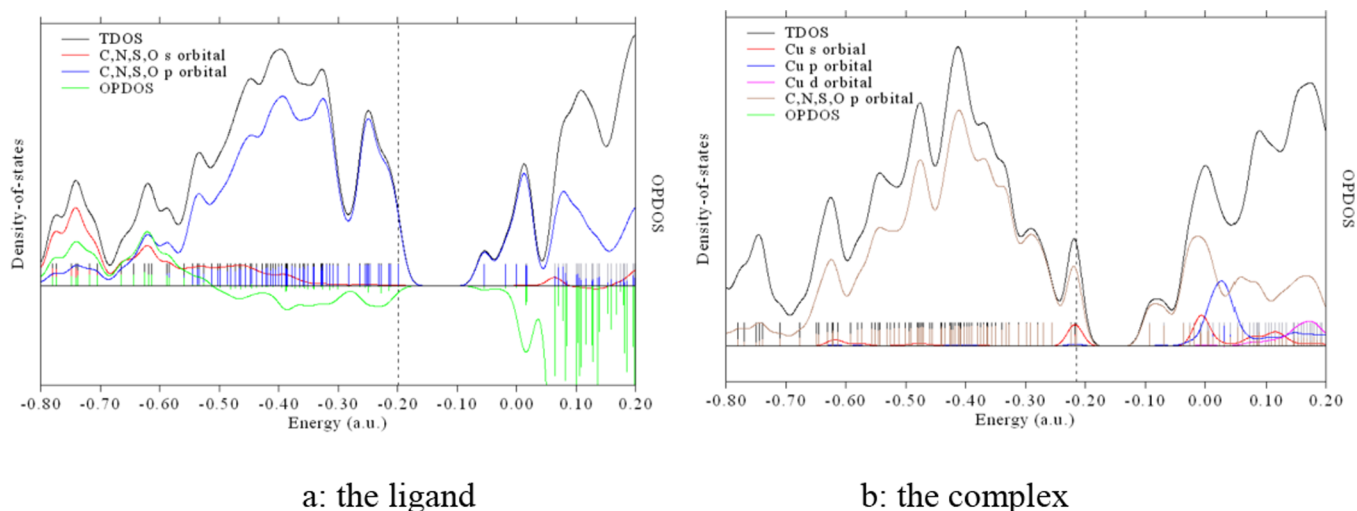
a: the ligand   b: the complex

Figure 7. DOS map (curve) and PDOS of the title compounds. The location of the HOMO is displayed by a black dashed line.

(TDOS) map of the ligand MOs and its partial DOS (PDOS) maps are nearly contributed by p orbitals of the carbon, nitrogen, sulfur, and oxygen atoms. Figure 7 clearly shows as well that the TDOS of several frontier molecular orbitals are completely composed of the p orbitals of the non-hydrogen atoms, making their PDOS curves strongly overlap with DOS. For the complex, due to addition of the Cu(II) cation, its HOMO and LUMO mainly consist of the s orbital from the copper cation and the p orbitals from the ligand atoms. The p and d orbitals of the Cu(II) cation only contribute to the higher unoccupied MOs and almost do not contribute to the occupied orbitals. By looking at Figure 7a,b, we can see that the p orbitals from the non-hydrogen atoms play a key pole in their DOS and PDOS diagrams, whether the ligand or the complex. The calculated energies of the HOMO and the LUMO of both the ligand and the complex are found to be −5.42 and −5.84 eV and −1.48 and −3.81 eV, respectively, corresponding to the HOMO−LUMO gap of 3.94 and 2.03 eV. This observation implies that the addition of the s orbital from Cu(II) lowers the frontier molecular orbitals of the complex; However, its LUMO is decreased more than the HOMO; therefore, the HOMO−LUMO gap of the complex is smaller compared with that of the ligand. Also, it is important to emphasize that the overlap integral of the HOMO and LUMO becomes smaller due to the mixed s-orbital from the copper cation.

In order to investigate the bonding situation between the central ion and the ligand, we calculated the bond order of each chemical bond in this complex by the Fuzzy bond order analysis.[33] From Figure S5, it can be seen that the bond order of the chemical bond (0.401 and 0.476) formed between the two oxygen atoms and the copper ion is relatively large, while the bond order (0.394 and 0.379) formed between the two nitrogen atoms and the copper ion is relatively small. This indicates that the electron transfer of both the oxygen atoms in the ligand to the central ion is more than that from two nitrogen atoms. Moreover, we found that the coordination bond formed between the oxygen atom from the carboxyl group and the central ion is the strongest, so the bond length is the shortest and the bond order is the highest.

4. CONCLUSIONS

In this paper, we employed DFT/TDDFT and MOMAP program to investigate theoretically the photophysical properties of a highly selective probe for copper(II) detection. The peptide-modified dansyl fluorescent probe has been shown to turn on in response to Cu^{2+} experimentally. For the probe molecule, the accurate calculation of molecular response properties indicated that the oscillator strength of the maximum emission peak in the fluorescent process is considerably large, but the counterpart of its copper(II) complex is nearly zero. Therefore, the predicted radiative rate k_r of the probe is several orders of magnitude larger than that of its complex; however, the predicted internal conversion rate k_{ic} of both the probe and its complex is of the same order of magnitude. In addition, the simulated ISC rate k_{isc} of the complex is much greater than that of the probe due to the effect of heavy atom from the copper atom in the complex. Based on the above information, the calculated fluorescence quantum yield of the probe is 0.16% and that of the complex is 10^{-6}%, which implies that the first excited state of the probe is bright state and that of the complex is dark state. For the complex, the hole−electron pair analysis indicated that the process of $S_0 \rightarrow S_1$ belongs to metal-to-ligand charge transfer. Its DOS diagram visually illustrates that the HOMO contains the ingredient of the s orbital from the copper atom, which decreases the frontier orbital energy level and the overlap integral of HOMO and LUMO.

■ ASSOCIATED CONTENT

ⓢ Supporting Information

The Supporting Information is available free of charge at https://pubs.acs.org/doi/10.1021/acsomega.3c01528.

Both the dihedral angles in S_0 and S_1 states for the ligand by B3LYP/6-31G(d,p), bond parameters of the studied molecule in their S_0 states by ωB97XD/6-31G(d,p), structures, inner energy, and percentage via Boltzmann statistics of the complex isomers by B3LYP/GEN, first four largest reorganization energies corresponding to vibrational modes at S_1 states for the studied molecules, simulated Fuzzy bond order in the complex, calculated frequencies of the title compound with PCM, reorganization energy (λ_k/cm^{-1}), Huang−Rhys factor (S_k), and

nonadiabatic coupling matrix element (R) of $S_1 \rightarrow S_0$ (PDF)

■ AUTHOR INFORMATION

Corresponding Authors

Huixue Li − School of Chemical Engineering and Technology, Tianshui Normal University, Tianshui, Gansu 741001, China; orcid.org/0000-0002-7467-9090; Phone: +86-15097274526; Email: li_hx2001@126.com

Zhifeng Li − School of Chemical Engineering and Technology, Tianshui Normal University, Tianshui, Gansu 741001, China; Email: lizhfe2003@163.com

Authors

Xiaofeng Wang − School of Chemical Engineering and Technology, Tianshui Normal University, Tianshui, Gansu 741001, China

Kun Yuan − School of Chemical Engineering and Technology, Tianshui Normal University, Tianshui, Gansu 741001, China

Lingling Lv − School of Chemical Engineering and Technology, Tianshui Normal University, Tianshui, Gansu 741001, China

Kui Liu − School of Chemical Engineering and Technology, Tianshui Normal University, Tianshui, Gansu 741001, China

Complete contact information is available at:
https://pubs.acs.org/10.1021/acsomega.3c01528

Notes

The authors declare no competing financial interest.

■ REFERENCES

(1) Nan, X.; Huyan, Y.; Li, H.; Sun, S.; Xu, Y. Reaction-based fluorescent probes for Hg²⁺, Cu²⁺ and Fe³⁺/Fe²⁺. *Coordin. Chem. Rev.* **2021**, *426*, No. 213580.

(2) (a) Chang, Y.; Fu, J.; Yao, K.; Li, B.; Xu, K.; Pang, X. Novel fluorescent probes for sequential detection of Cu²⁺ and citrate anion and application in living cell imaging. *Dyes Pigm.* **2019**, *161*, 331−340. (b) Cheng, W.; Xie, Y.; Yang, Z.; Sun, Y.; Zhang, M. Z.; Ding, Y.; Zhang, W. General Strategy for in Situ Generation of a Coumarin-Cu²⁺ Complex for Fluorescent Water Sensing. *Anal. Chem.* **2019**, *91*, 5817−5823. (c) Feng, Y.; Yang, Y.; Wang, Y.; Qiu, F.; Song, X.; Tang, X.; Zhang, G.; Liu, W. Dual-functional colorimetric fluorescent probe for sequential Cu²⁺ and S²⁻ detection in bio-imaging. *Sens. Actuators, B* **2019**, *288*, 27−37.

(3) Gu, Y. Q.; Shen, W. Y.; Zhou, Y.; Chen, S. F.; Mi, Y.; Long, B.-F.; Young, D. J.; Hu, F. L. A pyrazolopyrimidine based fluorescent probe for the detection of Cu²⁺ and Ni²⁺ and its application in living cells. *Spectrochim. Acta, Part A* **2019**, *209*, 141−149.

(4) (a) Duan, Y. W.; Tang, H. Y.; Guo, Y.; Song, Z. K.; Peng, M. J.; Yan, Y. The synthesis and study of the fluorescent probe for sensing Cu²⁺ based on a novel coumarin Schiff-base. *Chin. Chem. Lett.* **2014**, *25*, 1082−1086. (b) Wu, F. Y.; Cao, S. G.; Xie, C. X. A highly selective chemosensor for copper ion based on ICT fluorescence. *Chin. Chem. Lett.* **2012**, *23*, 607−610.

(5) (a) Wang, L.; Cao, H.-X.; He, Y. S.; Pan, C. G.; Sun, T. K.; Zhang, X. Y.; Wang, C. Y.; Liang, G. X. Facile preparation of amino-carbon dots/gold nanoclusters FRET ratiometric fluorescent probe for sensing of Pb²⁺/Cu²⁺. *Sens. Actuators, B* **2019**, *282*, 78−84. (b) Royzen, M.; Dai, Z.; Canary, J. W. Ratiometric Displacement Approach to Cu(II) Sensing by Fluorescence. *J. Am. Chem. Soc.* **2005**, *127*, 1612−1613.

(6) (a) Hien, N. K.; Bay, M. V.; Bao, N. C.; Vo, Q. V.; Cuong, N. D.; Thien, T. V.; Nhung, N. T. A.; Van, D. U.; Nam, P. C.; Quang, D. T. Coumarin-Based Dual Chemosensor for Colorimetric and Fluorescent Detection of Cu²⁺ in Water Media. *ACS Omega* **2020**, *5*, 21241−21249. (b) Zhang, D.; Wang, Z.; Yang, J.; Yi, L.; Liao, L.; Xiao, X. Development of a method for the detection of Cu²⁺ in the environment and live cells using a synthesized spider web-like fluorescent probe. *Biosens. Bioelectron.* **2021**, *182*, No. 113174. (c) Sakunkaewkasem, S.; Petdum, A.; Panchan, W.; Sirirak, J.; Charoenpanich, A.; Sooksimuang, T.; Wanichacheva, N. Dual-Analyte Fluorescent Sensor Based on [5]Helicene Derivative with Super Large Stokes Shift for the Selective Determinations of Cu²⁺ or Zn²⁺ in Buffer Solutions and Its Application in a Living Cell. *ACS Sens.* **2018**, *3*, 1016−1023.

(7) Liu, Y.; Jiang, B.; Zhao, L.; Zhao, L.; Wang, Q.; Wang, C.; Xu, B. A dansyl-based fluorescent probe for sensing Cu²⁺ in aqueous solution. *Spectrochim. Acta, Part A* **2021**, *261*, No. 120009.

(8) Wu, W.; Min, S.; Tong, Q.; Wang, J.; Hu, J.; Dhamsaniya, A.; Shah, A. K.; Mehta, V. P.; Dong, B.; Song, B. Highly sensitive and selective "turn-off" fluorescent probes based on coumarin for detection of Cu²⁺. *Colloid Interface Sci. Commun.* **2021**, *43*, No. 100451.

(9) (a) Zhao, Y. H.; Luo, Y.; Wang, H.; Wei, H.; Guo, T.; Tan, H.; Yuan, L.; Zhang, X. B. A novel ratiometric and reversible fluorescence probe with a large Stokes shift for Cu2+ based on a new clamp-on unit. *Anal. Chim. Acta* **2019**, *1065*, 134−141. (b) Wang, L.; Li, M.; Li, W.; Han, Y.; Liu, Y.; Li, Z.; Zhang, B.; Pan, D. Rationally designed efficient dual-mode colorimetric/fluorescence sensor based on carbon dots for detection of ph and Cu²⁺ ions. *ACS Sustainable Chem. Eng.* **2018**, *6*, 12668−12674. (c) Sharma, A. K.; Priya; Kaith, B. S.; Isha; Singh, A.; Chandel, K.; Vipula. Riboflavin functionalized dextrin-sodium alginate based fluorescent sensor: detoxification of Cu²⁺ and Ni²⁺ Ions. *ACS Appl. Polym. Mater.* **2019**, *1*, 3084−3094.

(10) (a) Han, X.; Gu, C.; Ding, Y.; Yu, J.; Li, K.; Zhao, D.; Chen, B. Stable Eu³⁺/Cu²⁺-functionalized supramolecular zinc(ii) complexes as fluorescent probes for turn-on and ratiometric detection of hydrogen sulfide. *ACS Appl. Mater. Interfaces* **2021**, *13*, 20371−20379. (b) Bai, C.; Zhang, J.; Qin, Y.; Meng, Q.; Yao, J.; Huang, H.; Wei, B.; Li, R.; Zhang, L.; Miao, H.; et al. Strategy for detecting carbon monoxide: Cu²⁺-assisted fluorescent probe and its applications in biological imaging. *Anal. Chem.* **2022**, *94*, 11298−11306. (c) Chen, J.; Chen, H.; Wang, T.; Li, J.; Wang, J.; Lu, X. Copper ion fluorescent probe based on Zr-MOFs composite material. *Anal. Chem.* **2019**, *91*, 4331−4336.

(11) Yang, X.; Zhang, D.; Ye, Y.; Zhao, Y. Recent advances in multifunctional fluorescent probes for viscosity and analytes. *Coordin. Chem. Rev.* **2022**, *453*, No. 214336.

(12) (a) Cao, X.; Gao, Q.; He, X.; Bai, Y.; Sun, W. A colorimetric probe for detection of Cu²⁺by the naked eye and application in test paper. *Luminescence* **2020**, *35*, 651−658. (b) Kaur, M.; Choi, D. H. Diketopyrrolopyrrole: brilliant red pigment dye-based fluorescent

probes and their applications. *Chem. Soc. Rev.* **2015**, *44*, 58−77. (c) Wang, S.; Ding, H.; Wang, Y.; Fan, C.; Liu, G.; Pu, S. A colorimetric and ratiometric fluorescent sensor for sequentially detecting Cu²⁺ and arginine based on a coumarin−rhodamine B derivative and its application for bioimaging. *RSC Adv.* **2019**, *9*, 6643−6649.

(13) (a) Haiyan, W.; Shun, Y.; Qian, L.; Kun, W.; Haizhu, Y. Theoretical exploration for recognition mechanism of two similar coumarin-based probes on Hg²⁺ and Cu²⁺. *J. Mol. Struct.* **2019**, *1198*, 126870−126870. (b) Walter, E. D.; Stevens, D. J.; Visconte, M. P.; Millhauser, G. L. The prion protein is a combined zinc and copper binding protein: Zn²⁺ alters the distribution of Cu²⁺ coordination modes. *J. Am. Chem. Soc.* **2007**, *129*, 15440−15441.

(14) (a) Li, F.; Sa, R. Formation of Cu3,4(TCA), making the TCA complex a highly selective probe for Cu²⁺ detection: a TDDFT study. *J. Mater. Chem. C* **2019**, *7*, 2443−2456. (b) Xue, Y.; Liu, Y.; Wang, G.; An, L.; Teng, Y.; Chen, M.; Xie, Y.; Zhang, L. TDDFT study on the photophysical properties of coumarinyl chalcones and sensing mechanism of a derived fluorescent probe for hydrogen sulfide. *Spectrochim. Acta, Part A* **2020**, *234*, No. 118263. (c) Min, C.-G.; Liu, Q. B.; Leng, Y.; Huang, S. J.; Liu, C. X.; Yang, X. K.; Ren, A. M.; Pinto da Silva, L. Development of firefly oxyluciferin derivatives as pH sensitive fluorescent Probes: A DFT/TDDFT study. *Comput. Theor. Chem.* **2018**, *1133*, 18−24.

(15) Li, G. Y.; Han, K. L. The sensing mechanism studies of the fluorescent probes with electronically excited state calculations. *Wiley Interdiscip. Rev.: Comput. Mol. Sci.* **2018**, *8*, No. e1351.

(16) (a) Bhat, H. R.; Jha, P. C. Cyanide anion sensing mechanism of 1,3,5,7-tetratolyl aza-BODIPY: Intramolecular charge transfer and partial configuration change. *Chem. Phys. Lett.* **2017**, *669*, 9−16. (b) Basheer, S. M.; Sreekanth, A. TD-DFT study on the fluoride and copper ion sensing mechanism of pyrene N(4) phenyl thiosemi-carbazone. *Comput. Theor. Chem.* **2016**, *1085*, 31−39. (c) Sun, X. F.; Zhang, Z. X.; Li, W.; Bai, F.; Wang, J.; Jia, R.; Kong, C. P.; Zhang, H. X. DFT/TD-DFT calculations on the sensing mechanism of a dual response near-infrared fluorescent chemosensor for superoxide anion and hydrogen polysulfides: photoinduced electron transfer. *RSC Adv.* **2016**, *6*, 104735−104741.

(17) Lu, T. Molclus program, Version 1.9.9.9. http://www.keinsci.com/research/molclus.html (accessed September 2022).

(18) (a) Korth, M. Third-generation hydrogen-bonding corrections for semiempirical QM methods and force fields. *J. Chem. Theory Comput.* **2010**, *6*, 3808−3816. (b) Stewart, J. J. P. MOPAC, 2016; S. C.; Chemistry: Colorado Springs, CO, 2016.

(19) Frisch, M. J.; Trucks, G. W.; Schlegel, H. B.; Scuseria, G. E.; Robb, M. A.; Cheeseman, J. R.; Scalmani, G.; Barone, V.; Petersson, G. A.; Nakatsuji, H.; Li, X.; Caricato, M.; Marenich, A. V.; Bloino, J.; Janesko, B. G.; Gomperts, R.; Mennucci, B.; Hratchian, H. P.; Ortiz, J. V.; Izmaylov, A. F.; Sonnenberg, J. L.; Williams-Young, D.; Ding, F.; Lipparini, F.; Egidi, F.; Goings, J.; Peng, B.; Petrone, A.; Henderson, T.; Ranasinghe, D.; Zakrzewski, V. G.; Gao, J.; Rega, N.; Zheng, G.; Liang, W.; Hada, M.; Ehara, M.; Toyota, K.; Fukuda, R.; Hasegawa, J.; Ishida, M.; Nakajima, T.; Honda, Y.; Kitao, O.; Nakai, H.; Vreven, T.; Throssell, K.; Montgomery, Jr., J. A.; Peralta, J. E.; Ogliaro, F.; Bearpark, M. J.; Heyd, J. J.; Brothers, E. N.; Kudin, K. N.; Staroverov, V. N.; Keith, T. A.; Kobayashi, R.; Normand, J.; Raghavachari, K.; Rendell, A. P.; Burant, J. C.; Iyengar, S. S.; Tomasi, J.; Cossi, M.; Millam, J. M.; Klene, M.; Adamo, C.; Cammi, R.; Ochterski, J. W.; Martin, R. L.; Morokuma, K.; Farkas, O.; Foresman, J. B.; Fox, D. J. Gaussian, Inc.: Wallingford, CT, 2016.

(20) (a) Li, S. J.; Lan, Y. Is Cu (iii) a necessary intermediate in Cu-mediated coupling reactions? A mechanistic point of view. *Chem. Commun.* **2020**, *56*, 6609−6619. (b) Liang, P.; Kobayashi, A.; Sameera, W. M. C.; Yoshida, M.; Kato, M. Solvent-free thermal synthesis of luminescent dinuclear Cu(I) complexes with triarylphosphines. *Inorg. Chem.* **2018**, *57*, 5929−5938.

(21) (a) Mennucci, B. Polarizable continuum model. *Wiley Interdiscip. Rev.: Comput. Mol. Sci.* **2012**, *2*, 386−404. (b) Cossi, M.; Barone, V.; Cammi, R.; Tomasi, J. Ab initio study of solvated

molecules: a new implementation of the polarizable continuum model. *Chem. Phys. Lett.* **1996**, *255*, 327−335.

(22) Niu, Y.; Li, W.; Peng, Q.; Geng, H.; Yi, Y.; Wang, L.; Nan, G.; Wang, D.; Shuai, Z. MOlecular MAterials Property Prediction Package (MOMAP) 1.0: a software package for predicting the luminescent properties and mobility of organic functional materials. *Mol. Phys.* **2018**, *116*, 1078−1090.

(23) (a) Li, H.; Wang, X.; Yuan, K.; Lv, L.; Li, Z. Insights from QM/MM-ONIOM calculations: the TADF phenomenon of phenanthro-[9,10-d]imidazole-anthraquinone in the solid state. *Phys. Chem. Chem. Phys.* **2021**, *23*, 20218−20229. (b) Wang, Y.; Peng, Q.; Shuai, Z. A computational scheme for evaluating the phosphorescence quantum efficiency: applied to blue-emitting tetradentate Pt(II) complexes. *Mater. Horiz.* **2022**, *9*, 334−341.

(24) (a) Li, S.; Jin, X.; Yu, Z.; Xiao, X.; Geng, H.; Liao, Q.; Liao, Y.; Wu, Y.; Hu, W.; Fu, H. Design of thermally activated delayed fluorescent emitters for organic solid-state microlasers. *J. Mater. Chem. C* **2021**, *9*, 7400−7406. (b) Lin, S.; Ou, Q.; Shuai, Z. Computational selection of thermally activated delayed fluorescence (TADF) molecules with promising electrically pumped lasing property. *ACS Mater. Lett.* **2022**, *4*, 487−496. (c) Wang, M.; Wang, Y.; Hu, R.; Li, R.; Shuai, Z.; Wei, Y. AIEgens with cyano-modification in different sites: Potential 'Meta-site effect' in mechanochromism behavior. *Dyes Pigm.* **2022**, *198*, No. 109939.

(25) Smolentsev, G.; Milne, C. J.; Guda, A.; Haldrup, K.; Szlachetko, J.; Azzaroli, N.; Cirelli, C.; Knopp, G.; Bohinc, R.; Menzi, S.; et al. Taking a snapshot of the triplet excited state of an OLED organometallic luminophore using X-rays. *Nat. Commun.* **2020**, *11*, 2131.

(26) Costa, R.; Reta, D.; Moreira, I.; Illas, F. d. P. R. Post-B3LYP functionals do not improve the description of magnetic coupling in Cu (II) dinuclear complexes. *J. Phys. Chem. A* **2018**, *122*, 3423−3432.

(27) Gao, Z.; Chen, S.; Bai, Y.; Wang, M.; Liu, X.; Yang, W.; Li, W.; Ding, X.; Yao, J. A new perspective for evaluating the photoelectric performance of organic−inorganic hybrid perovskites based on the DFT calculations of excited states. *Phys. Chem. Chem. Phys.* **2021**, *23*, 11548−11556.

(28) Bekker, T. B.; Yelisseyev, A. P.; Solntsev, V. P.; Davydov, A. V.; Inerbaev, T. M.; Rashchenko, S. V.; Kostyukov, A. I. The influence of co-doping on the luminescence and thermoluminescence properties of Cu-containing fluoride borate crystals. *CrystEngComm* **2021**, *23*, 6599−6609.

(29) (a) Santiago, P. H. O.; Tiago, F. S.; Castro, M. S.; Souza, P. E. N.; Martins, J. B. L.; Gatto, C. C. DFT analysis, spectroscopic study and biological activity of a newly synthesized benzoylhydrazone binuclear Cu (II) complex. *J. Inorg. Biochem.* **2020**, *204*, No. 110949. (b) Chen, L.; Janssens, T. V. W.; Grönbeck, H. A comparative test of different density functionals for calculations of NH 3-SCR over Cu-Chabazite. *Phys. Chem. Chem. Phys.* **2019**, *21*, 10923−10930. (c) Sciortino, G.; Lubinu, G.; Maréchal, J. D.; Garribba, E. DFT Protocol for EPR prediction of paramagnetic Cu (II) complexes and application to protein binding sites. *Magnetochemistry* **2018**, *4*, 55.

(30) (a) López-Estrada, O.; Laguna, H. G.; Barrueta-Flores, C.; Amador-Bedolla, C. Reassessment of the four-point approach to the electron-transfer marcus−hush theory. *ACS Omega* **2018**, *3*, 2130−2140. (b) Li, H.; Duan, L.; Zhang, D.; Qiu, Y. Influence of molecular packing on intramolecular reorganization energy: a case study of small molecules. *J. Phys. Chem. C* **2014**, *118*, 14848−14852.

(31) Liu, Z.; Lu, T.; Chen, Q. An sp-hybridized all-carboatomic ring, cyclo[18]carbon: Bonding character, electron delocalization, and aromaticity. *Carbon* **2020**, *165*, 468−475.

(32) Lu, T.; Chen, F. Multiwfn: A multifunctional wavefunction analyzer. *J. Comput. Chem.* **2012**, *33*, 580−592.

(33) Lu, T. Multiwfn manual, Section 3.1.2. Available at http://sobereva.com/multiwfn/ (accessed August 2022).